communications physics

A Nature Portfolio journal

Article

https://doi.org/10.1038/s42005-025-02242-7

Flux-periodic supercurrent oscillations in an Aharonov–Bohm-type nanowire Josephson junction

Patrick Zellekens[1,7] ✉, Russell S. Deacon[1,2], Farah Basaric[3,4], Raghavendra Juluri[5], Michael D. Randle[2], Benjamin Bennemann[4,6], Christoph Krause[4,6], Erik Zimmermann[3,4], Ana M. Sanchez[5], Detlev Grützmacher[3,4], Alexander Pawlis[4,6], Koji Ishibashi[1,2] & Thomas Schäpers[3,4]

Recent theoretical studies highlight hollow-core semiconductor-superconductor hybrid nanowires as a promising platform to engineer topological superconductivity via the Little-Parks effect and phase-winding of the superconducting order parameter. Such nanowires exhibit enhanced spatial confinement of carriers, potentially enlarging the accessible topological phase space compared to conventional core/full-shell structures. Inspired by these insights and as an essential preliminary step, we experimentally investigate GaAs/InAs core/shell nanowires with aluminum half-shells, aiming to understand how Andreev-bound states are influenced by their complex geometric confinement. With normal contacts we observed pronounced *h/e* flux periodic oscillations in the magnetoconductance, which can be explained via the presence of a tubular conductive channel in the InAs shell. Conversely, the switching current in Josephson junctions oscillates with approximately half that period, i.e., *h/2e*, indicating a full proximitization of the InAs shell from the half-shell superconducting contacts and a successful imprint of the non-trivial geometric topology onto the Andreev transport spectrum in the junction enclosing threading magnetic flux. On these structures, we systematically studied the gate-, field-, and temperature-dependent evolution of the supercurrent.

Josephson junctions, at their core, are two superconductors separated by a thin insulating barrier or a weak link. They allow the dissipationless and coherent transfer of bosonic quasiparticles, i.e., Cooper pairs. The resulting supercurrent flows without the application of an external voltage and is only driven by the phase difference between the macroscopic wavefunctions in the superconducting electrodes, i.e., the Josephson effect.

Realizations of such devices with a semiconductor nanowire (NW) as the weak link have generated significant attention for their potential in the realization of superconducting quantum circuits, particularly within the realm of quantum computing. The appeal of these junctions lies in their multifaceted advantages. Firstly, the incorporation of a semiconducting weak link enables precise control of junction parameters through field-effect manipulation. This attribute permits dynamic adjustments of the quantum circuit's properties, making it a flexible platform for quantum information processing. Secondly, the unique combination of a large Fermi wavelength and a small nanowire diameter enables the design of junctions wherein only a limited subset of quantum states, known as Andreev bound states, play a pivotal role in carrying the Josephson supercurrent[1–3]. This selective modulation facilitates the use of paired Andreev bound states as a foundational element for the creation of quantum bits (qubits)[4–8], which are the fundamental units of quantum information processing.

Moreover, semiconductor nanowire hybrid structures play a central role in the quest for realizing topological qubits[9–11], a cutting-edge approach to fault-tolerant quantum computing beyond the current NISQ (noisy-intermediate-scale-quantum) methodology. Here, qubits are constructed based on the unique properties of topological states of matter, which offer inherent protection against certain types of quantum errors, thus rising the fidelity of the whole system. A key element in this endeavor is the search for parafermionic excitations, e.g., Majorana zero modes (MZMs)[9,12]. The latter

[1]RIKEN Center for Emergent Matter Science, Wako, Japan. [2]Advanced Device Laboratory, RIKEN, Wako, Japan. [3]Peter Grünberg Institut 9, Forschungszentrum Jülich, Jülich, Germany. [4]JARA-Fundamentals of Future Information Technology, Jülich-Aachen Research Alliance, Forschungszentrum Jülich and RWTH Aachen University, Jülich, Germany. [5]Department of Physics, University of Warwick, Coventry, UK. [6]Peter Grünberg Institut 10, Forschungszentrum Jülich, Jülich, Germany. [7]Present address: NTT Corporation, NTT Basic Research Laboratories, Atsugi, Japan. ✉e-mail: patrick.zellekens@ntt.com

are a particular type of quasiparticle excitation that behaves as its own antiparticle, i.e., with non-abelian characteristics. Thus, they are decoupled from the conventional charge carrier space, which makes them highly robust against external disturbances. Recently, several proposals have emerged that aim to overcome known challenges of trivial-topological phase transitions in hybrid nanowire Josephson junctions, e.g., the need for strong in-plane magnetic fields to open up a helical gap or large trivial charge carrier background contributions. In particular, the so-called Little-Parks effect in nanowire structures that are fully surrounded by a superconducting shell has gained considerable interest due to the much lower requirements in terms of magnetic field strength or the desired length of the Josephson junction channel[13–16]. The Little-Parks effect describes the periodic suppression and reemergence of superconductivity due to the acceleration and overheating of the Cooper pair condensate ($T_c \rightarrow 0$) in a thin-walled cylinder and a winding of the superconducting order parameter associated with it[17]. Such full-shell nanowire devices can display rich physics with analogs to Abrisokov vortices in type-II superconductors[18] and have application for flux control in Josephson devices[19].

Tunnel- and microwave spectroscopy studies in InAs/Al nanowire/full-shell devices confirmed the existence of the characteristic lobe structure of the Little-Parks effect, but did not find any clear evidence of MZMs or other topological excitations[20–22]. One possible cause for this is an insufficient radial quantization, which not only gives rise to a large number of possible angular momentum states, but might also still allow transport through the bulk of the nanowire[23].

By combining a wide bandgap core, e.g., GaAs, with a shell made out of a narrow bandgap material such as InAs, it is possible to confine the charge carriers and thereby enhance the radial quantization of the system. These core/shell systems cannot only act as Aharonov–Bohm (AB) type systems[24–27], but have also been studied in terms of an enlargement of the topological gap due to the steeper band bending, confinement, and wave function engineering, and an enhanced spin-orbit interaction[23,28–30]. In addition, these systems with an effectively "hollow" or "tubular" core[31–33] can be analytically mapped to the seminal models of Oreg et al.[10] and Lutchyn et al.[11]. Here, we take a step towards realizing these more complex systems by investigating epitaxially-grown GaAs/InAs/Al core/shell/half-shell nanowires that, in contrast to earlier works[34], have been fabricated by making use of state-of-the-art techniques such as self-catalyzed selective-area growth and an in-situ and low-temperature deposition of the superconducting shell[35–37].

First, information on orbital states present in the InAs shell is gained by measuring Aharanov–Bohm type oscillations on bare GaAs/InAs core/shell Nanowires. Subsequently, the characteristics of corresponding Josephson junctions are investigated. In particular, the periodic features present in the critical current are studied at various gate voltages, temperatures, and magnetic field orientations.

Results and discussion

Device details

The GaAs/InAs core/shell nanowires are grown selectively by molecular beam epitaxy (MBE) on pre-patterned substrates using the self-catalyzed vapor-liquid-solid method. Details about the nanowire growth can be found in the "Methods" section. In short, the polymorphic GaAs nanowires are grown selectively, resulting in a typical length of 4 µm and diameters between 100 and 200 nm (See Supplementary Notes 1 and 2 for details). Subsequently, the InAs shell is grown by vapor-solid overgrowth of the GaAs core. The total thickness of the InAs shell is about 20–30 nm. Two growth runs are performed with identical parameters. The nanowires of the first growth run are equipped with Ti/Au normal contacts for magneto-transport measurements (device A). In the second growth run, a 20–30 nm thick Al half-shell is in-situ deposited on the GaAs/InAs core/shell nanowire. In Fig. 1a, b, scanning electron microscope (SEM) images of front- and backside of the Al-half-shell covered GaAs/InAs nanowires are depicted. From this growth run two different Josephson junctions, i.e., devices B and C, have been fabricated and subsequently studied.

The structural properties of the GaAs/InAs/Al core/shell/half-shell nanowires are examined using scanning transmission electron microscopy (STEM) to generate both side and cross–section views. Figure 1c shows an annular dark field scanning transmission electron microscope (ADF-STEM) image of a GaAs/InAs/Al junction cross–section and the corresponding energy dispersive X-ray (EDX) elemental maps, which are given in Fig. 1e–h. The thicknesses of the different components were measured using several cross–sections. Based on that, we determined values of 150 nm, 25 nm, and 20 nm for the GaAs core, InAs, and Al half shell, respectively. Inspecting a magnified view (Fig. 1d) of the semiconductor/superconductor interface in the nanowire cross-section, we confirm a high level similar to

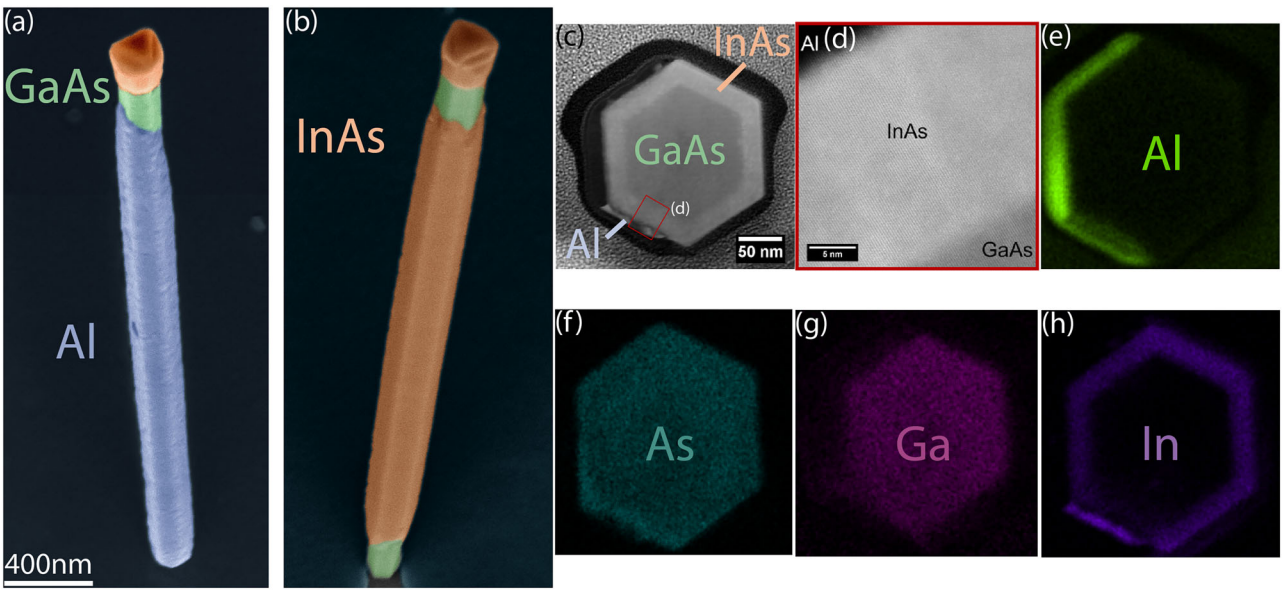

Fig. 1 | Structural and crystallographic analysis of GaAs/InAs/Al core/shell/halfshell nanowires. False-colored scanning electron micrographs of the **a** front- and **b** backside of a GaAs/InAs/Al core/shell/half-shell nanowire. **c** Annular dark-field scanning transmission electron micrograph (ADF-STEM) of a cross-section of one of the wires from (**a**), showing the hexagonal crystal structure. **d** Zoom-in of the area outlined in red in (**c**), revealing a high InAs/Al interface quality. **e**–**h** Energy-dispersive X-ray spectroscopy (EDX) analysis of the same nanowire.

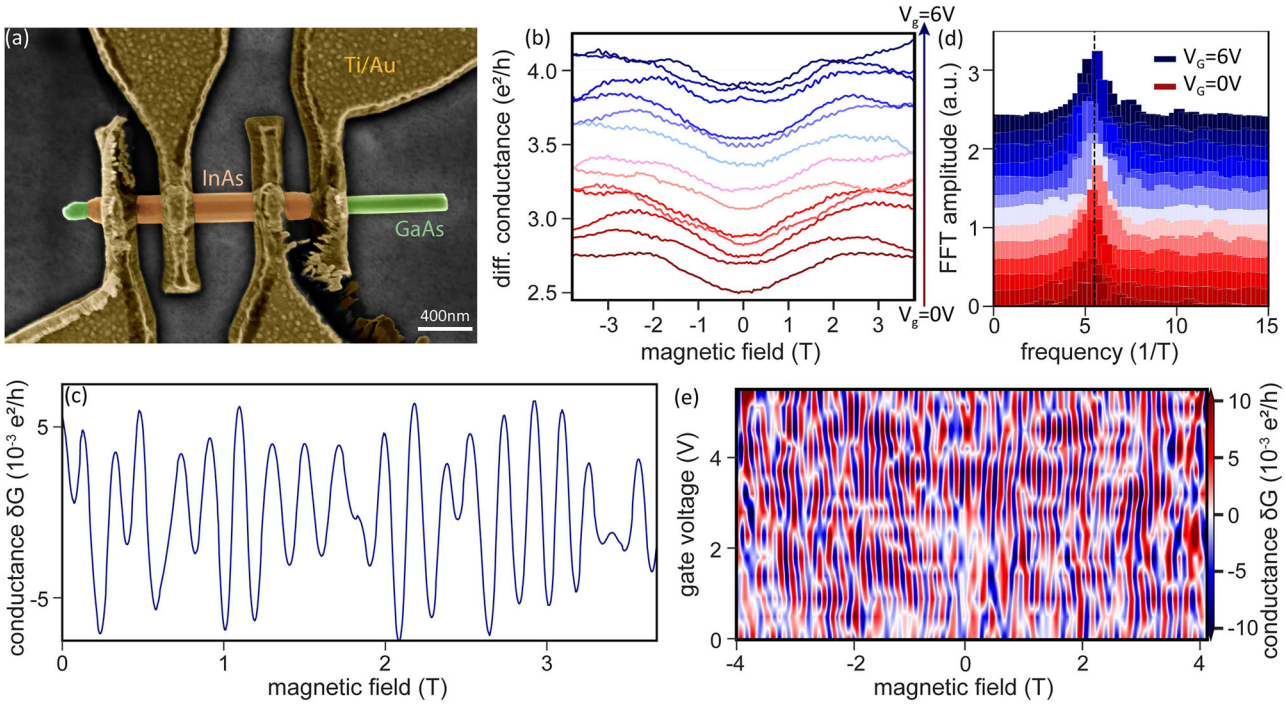

Fig. 2 | Flux-periodic magnetoconductance oscillations in a GaAs/InAs core/shell nanowire with normal contacts. a Scanning electron micrograph of GaAs/InAs core/shell nanowire (green/orange) equipped with normal conducting Ti/Au contacts (device A). **b** Magnetoconductance in units of e^2/h of device A at various gate voltages between 0 and 6 V (0.5 V steps). **c** Conductance in units of e^2/h at 1.7 K and $V_g = 6$ V after subtracting the slowly varying background signal. **d** Fast-Fourier transformation of the measurements shown in (**b**). **e** Conductance as a function of magnetic field and gate voltage, showing the evolution of the oscillation phase.

what is reported for conventional InAs nanowires with in-situ Al[35,37]. Lastly, the EDX maps of Fig. 1e–h depict the chemical composition of the nanowires, confirming no signs of obvious (inter-)diffusion of elements. Further TEM images of the Al/InAs interface and an intensity profile across the GaAs/InAs/Al heterostructure can be found in the Supplementary Note 1, Figs. S1 and S2.

Magnetoconductance in GaAs/InAs core/shell nanowires

First, the transport properties of bare core/shell GaAs/InAs NWs are studied. Figure 2a shows an SEM image of the normal contacted sample (device A) made with wires from the first growth run. In this device, the GaAs core has a diameter of 150 nm and an InAs shell thickness of 25 nm. To confirm the phase–coherent nature of electronic transport at low temperatures, the conductance of device A was measured under an axially applied magnetic field B at gate voltages (V_g) between 0 and 6 V. In the obtained curves, we observe regular h/e–periodic oscillations in the conductance G (cf. Fig. 2b), which are attributed to AB–type oscillations[24]. The oscillation amplitude is about 0.5% of the total conductance and does not exhibit a significant increase for higher gate voltages and enhanced electron accumulation[24]. In order to better resolve the oscillation pattern, the slowly varying background $G_0(B)$ was subtracted from the conductance by means of a moving average fit, resulting in the oscillation signal $\delta G = G - G_0(B)$ plotted exemplary in Fig. 2c for $V_g = 6$ V. The beating pattern in the signal is attributed to small radius variations along the nanowire axis and hence its enclosed area A, resulting in differences of the enclosed magnetic flux $\Phi = AB$. In addition, we observe a decrease of the oscillation amplitude with temperature increase (See Supplementary Note 3 and Fig. S3)[27], which is consistent with a reduction of the phase-coherence length due to thermally induced scattering events. Figure 2d shows the fast-Fourier transform (FFT) amplitudes for various gate voltages corresponding to the recorded magnetoconductance oscillations shown in (b). The central frequency peak occurring at 5.5 T^{-1} implies oscillation period of $\Delta B \approx 182$ mT. Assuming a hexagonal cross-sectional area of the nanowire and taking into account an estimated oscillation period ΔB, relation $h/e = \Delta B r^2 (3\sqrt{3}/2)$ yields a phase–coherent trajectory radius $r \approx 93$ nm. The obtained results imply a confined trajectory within the boundaries of the InAs shell and shows good agreement with the expected h/e-related frequency. This confirms that the origin of the observed Aharonov-Bohm type oscillations is that which one would expect of a tubular conductor[24,27]. Indeed, the radius calculated from the oscillation period agrees very well with the radius of 89 nm corresponding to a wave function located in the center of the InAs shell. Lastly, we studied the phase rigidity of the oscillations with respect to changes in the applied gate voltage. As can be seen in Fig. 2e, the oscillation phase is shifted when the gate voltage is varied. This behavior is a characteristic feature of AB-type oscillations in mesoscopic samples with disorder and can be attributed to different scattering paths around the circumference of the ring if the Fermi wavevector is changed[24,25,38].

Josephson junctions based on GaAs/InAs/Al core/shell/half-shell nanowires

After confirming the presence of phase-coherent transport via tubular states in normal contacted GaAs/InAs core/shell nanowires, we now focus on Josephson junctions based on corresponding core/shell nanowires with in-situ deposited Al half-shells. An example of such a device with an etched Josephson junction is shown in Fig. 3a (device B). As shown in Fig. 3b, for junction device B, a pronounced supercurrent with a switching current of $I_{sw}(V_g = 0\ \text{V}) = 22$ nA, and a normal state resistance (R_N) of about 2.2 kΩ is observed. Based on the hysteresis in the supercurrent branch (see inset), we determine that the junction is underdamped. In addition, the device exhibits several peaks in the differential resistance (red trace in Fig. 3b) that can be interpreted as signatures of multiple Andreev reflections[39,40]. For device C, the current-voltage characteristic shows a non-zero resistance in the supercurrent branch due to the presence of a parasitic series resistance of 273 Ω, the subtraction of which leads to a clear Josephson junction behavior, including the presence of well quantized Shapiro steps in AC-driven measurements (see Supplementary Note 4 and Fig. S4). We attribute this parasitic resistance to a poor connection between the superconducting Al shell and the superconducting NbTi leads due to an insufficient Ar cleaning

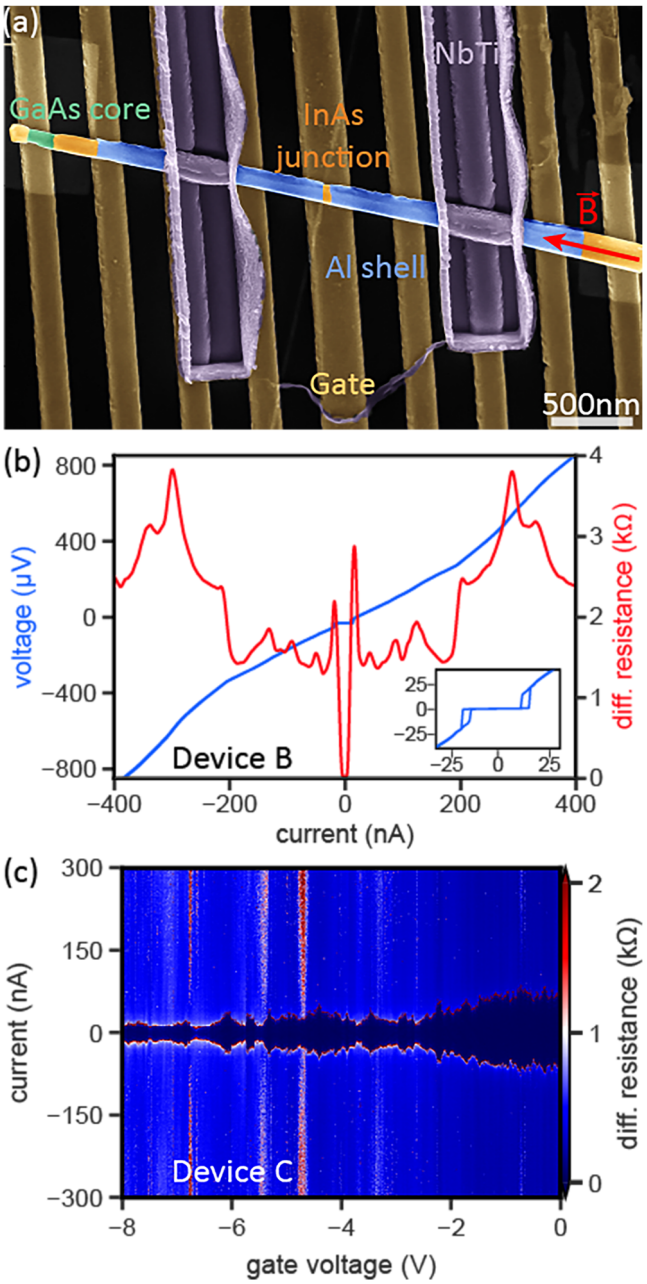

Fig. 3 | Supercurrent and Andreev transport in GaAs/InAs/Al Josephson junctions. a False-colored scanning electron micrograph of an exemplary GaAs/InAs/Al core/shell/halfshell nanowire Josephson junctions with an approx. 140 nm long channel. **b** Current-voltage characteristics (blue) and differential resistance (red) as a function of bias current of device B at $T = 14$ mK and a gate voltage of $V_g = 0$ V. The inset shows detail around the supercurrent branch of the I–V trace, revealing an underdamped behavior. **c** Differential resistance as a function gate voltage and bias current for device C at $T = 14$ mK.

process. As can be seen in Fig. 3c, for device C, the magnitude of the supercurrent as well as R_N can be altered by adjusting the gate voltage between $V_g = -8$ and 0 V. However, no complete pinch-off is achieved. We attribute this to the comparatively thick wire geometry, which lowers the effectiveness of the gate. Indeed, prior devices based on InAs/Al half-shell wires showed a full depletion of the conducting channel for negative gate voltages in the very same gate layout (c.f. ref. 41).

Following earlier experiments on core/shell nanowire devices[34,42], we focus on the modifications to the electrical transport if the device is penetrated by an in-plane magnetic field parallel to the nanowire axis. Figure 4a shows the change in differential resistance of the nanowire Josephson junction (device B) for an applied axial in-plane magnetic field and $V_g = -8$ V. In this configuration, the device exhibits the typical iris-shaped closing of the superconducting gap (see e.g., ref. 41) without any sign of additional quantum (interference) effects. However, for $V_g = 0$ V (see Fig. 4b), the response of the junction changes significantly. Here, both the supercurrent and the sub-gap Andreev transport start to show pronounced flux-periodic oscillations on top of the aforementioned closing of the superconducting gap (in the following referred to as background). The oscillations become even more prominent for large positive gate voltages ($V_g = 8$ V, c.f. Fig.4c). We also note that the oscillation spectrum extends all the way up into the dissipative regime, which might be relevant in the context of recent studies about Joule heating in nanowire-based hybrid junctions[43]. Figure 4d shows the extracted switching current (I_{sw}) of the junction, i.e., the current value above which the device starts to exhibit a finite resistance, as a function of magnetic field at several gate voltages for device B. For all gate voltages, we observe the previously mentioned iris-shaped background that is associated with the closing of the superconducting gap. However, above $V_g = 0$ V, flux-periodic oscillations of I_{sw} emerge, with a maximum amplitude at $V_g = 8$ V of ~1/4 of the zero-field background current. We note that the results are similar to a recent report in InAsSb/Al junctions where the surface accumulation layer provides a tubular channel[44]. However, the exact relation between the oscillation amplitude, background current, and tunability of their ratio remains unclear and requires further studies with different junction length and nanowire geometries.

In the case of the Josephson junction the highly visible oscillations allow simple extraction of the period, as shown in Fig. 4d, revealing $\Delta B \approx 60$ mT in device B. This value corresponds to an effective radii of $r_{h/e} \approx 158$ nm assuming h/e periodic oscillations or $r_{h/2e} \approx 112$ nm, assuming $h/2e$ periodic oscillations, for a hexagonal cross section. Based on an average total wire diameter of 300 nm, with an Al thickness of around $t_{Al} = 25$ nm and an InAs thickness of $t_{InAs} = 25$ nm and the fact that the maximum of the probability function is situated in the middle of the InAs shell[24], we find a good correspondence to the calculated effective radius $r_{h/2e}$. The relatively large difference to the cross-sectional dimensions of device A can be explained by the significant spread of nanowire GaAs core diameters between different arrays with holes of different diameters and pitches on the very same growth substrate (see Supplementary Note 2, Tables SI and SII for a more detailed analysis of the different nanowire dimensions across the growth substrates).

Figure 4e provides an overview of the gate- and magnetic field-dependent evolution of the switching current for device C. This device exhibits a region of suppressed I_{sw} (indicated by the arrow in Fig. 4e) that is hysteretic in magnetic field and we attribute to trapping of vortices within the junction[45]. Similar to results of device B, the depletion-induced damping of the flux-periodic oscillations is much stronger than one of the background supercurrent. Here, comparable radii as to device B are evaluated from the oscillation period of 60 mT with $r_{h/e} \approx 163$ nm or $r_{h/2e} \approx 115$ nm assuming h/e or $h/2e$ periodic oscillations, respectively. Contrary to the results for the normal conducting samples shown in Fig. 2e, fixed positions of the minima and maxima (see vertical lines in Fig. 4e) of the oscillations are observed. This resilience against changes in the applied gate voltage is a typical signature of quantum interference effects protected by time-reversal symmetry, such as $h/2e$-periodic Al'tshuler–Aronov–Spivak oscillations in normal conducting, mesoscopic samples[46], for which any effect of random scattering loops caused by modifications of the Fermi wave vector k_F, and thus the aforementioned additional phase shift, is canceled[46].

To gain a more detailed picture of the origin of the observed flux-periodic supercurrent oscillations in connection to the geometrical conditions, we investigate the transport in device C at temperatures above T_c of the aluminum half-shell and at bias voltages outside of the induced proximity gap, as shown in Fig. 5a–c, for $V_g = 0$ V, $V_g = 0$ V and $V_g = 8$ V, respectively. Figure 5a shows the evaluated switching current for $T = 14$ mK for comparison with traces in (b, c). Figure 5b shows the differential

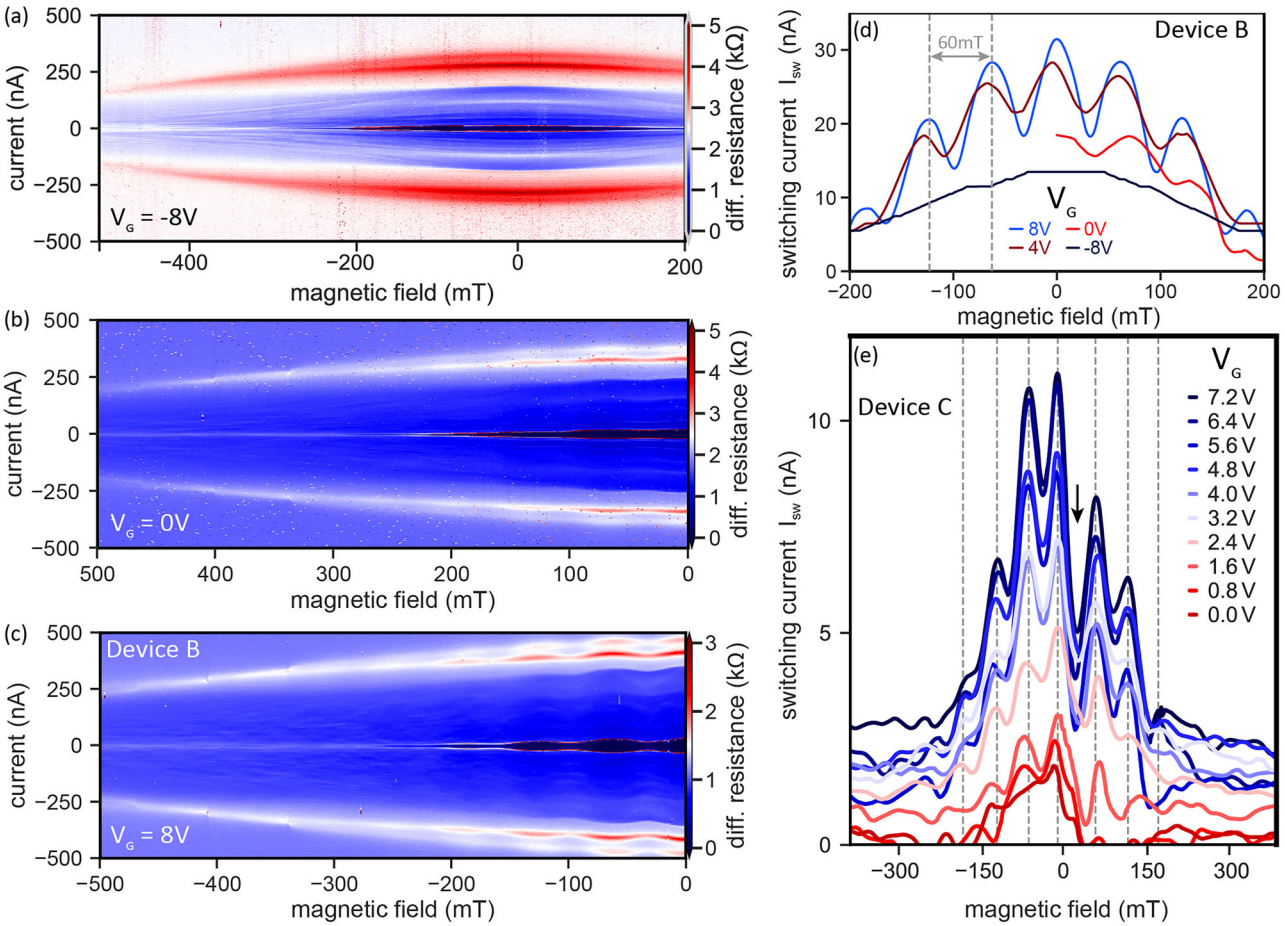

Fig. 4 | Flux-periodic supercurrent oscillations and their gate voltage dependence. a–c Differential resistance of device B as a function of magnetic field and bias current for $V_g = -8$ V, 0 V, and 8 V, respectively. **d** Switching current (I_{sw}) as a function of magnetic field evaluated for the gate voltages shown in (**a**–**c**). **e** Switching current of device C as a function of magnetic field (swept from negative to positive) at various gate voltages. Device C exhibits a narrow suppressed switching current feature that is hysteretic with respect to magnetic field and likely caused by trapping of vortices in the junction (indicated by an arrow).

resistance (dV/dI) measured at $T = 2.2$ K and at zero DC current ($I_{offset} = 0$), where the aluminum half-shell forming the junction is in the normal state ($T_c \sim 1$ K). Comparing the peak separation in (a, b), indicated by the dashed lines, one finds that the period of the oscillations approximately doubles if the transport takes place above the critical temperature of the aluminum half-shell. We also investigate how the system responds at temperatures for which the shell is superconducting ($T \ll T_c$) if subjected to bias currents that drive the transport into the dissipative regime. Using a superposition of a constant DC offset current of $I_{offset} = 600$ nA and a small AC lock-in signal, the resistivity oscillations shown in Fig. 5c reveal once more a prominent increase in their periodicity, as compared to the low-temperature and zero-bias response in Fig. 5a. We note that the period of oscillations in the superconducting transport is approximately 60 mT as compared to about 128 mT in the normal transport. Assuming that superconducting state oscillations are ($h/2e$) periodic and normal oscillations are (h/e) periodic this corresponds to radii of 115 and 112 nm, respectively.

The findings for the gate-, temperature-, and current-dependent evolution of the junction response indicate a clear correlation between the special device properties, i.e., the complex geometric topology, and the $h/2e$-oscillations. Furthermore, the observation of supercurrent oscillations goes beyond the earlier results reported in refs. 34,42,47 that were obtained on GaAs/InAs core/shell nanowire-based Josephson junctions with ex-situ contacts and global backgates and which could only observe the flux-periodic oscillations in the normal state resistance R_N. In this context, we interpret the results as an interference effect that takes place on the level of flux-periodic Andreev reflection/Andreev bound states within the nanowire. Following this picture, we assume that Andreev transport processes enclosing the threading flux can occur around the perimeter of the nanowire in regions without an aluminum shell. This is a strong indication that the InAs shell is fully proximitized in the aluminum-covered regions of the device. We expect that two effects may play a role in the device as discussed below. The first is based on the Little-Parks effect in an inhomogenous cylinder, in which most of the modulation of the superconducting order parameter occurs in the area with weaker superconductivity[48]. In this picture, the proximitized InAs shell on the side of the nanowire opposite the aluminum half-shell (i.e., the underside of the nanowire) forms an extended, additional weak-link that can support a non-zero non-dissipative current. Upon application of a field along the wire axis a screening current is induced around the wire circumference with a magnitude fixed by the current-phase relationship of this extended weak-link. The condensate velocity due to the screening current can then cause modulation of the critical temperature of the Al half-shell, akin to the Little-Parks effect, which in turn will modify the current that can be supported by the weak-link. In the conventional Little-Parks effect the screening current varies linearly with applied flux in contrast to the proposed sinusoidal variation due to the weak-link formation[49]. However, devices fabricated with normal contacts and no etched Josephson junction reveal no significant modulation of the superconducting transport (see Supplementary Note 5 and Fig. S6), indicating that the above-discussed effect, while possible, is likely not the primary cause of the strong modulation observed in the Josephson junction devices. Furthermore, the observed gate dependence gives a strong indication that the effect is likely specific to transport in vicinity of the defined junction.

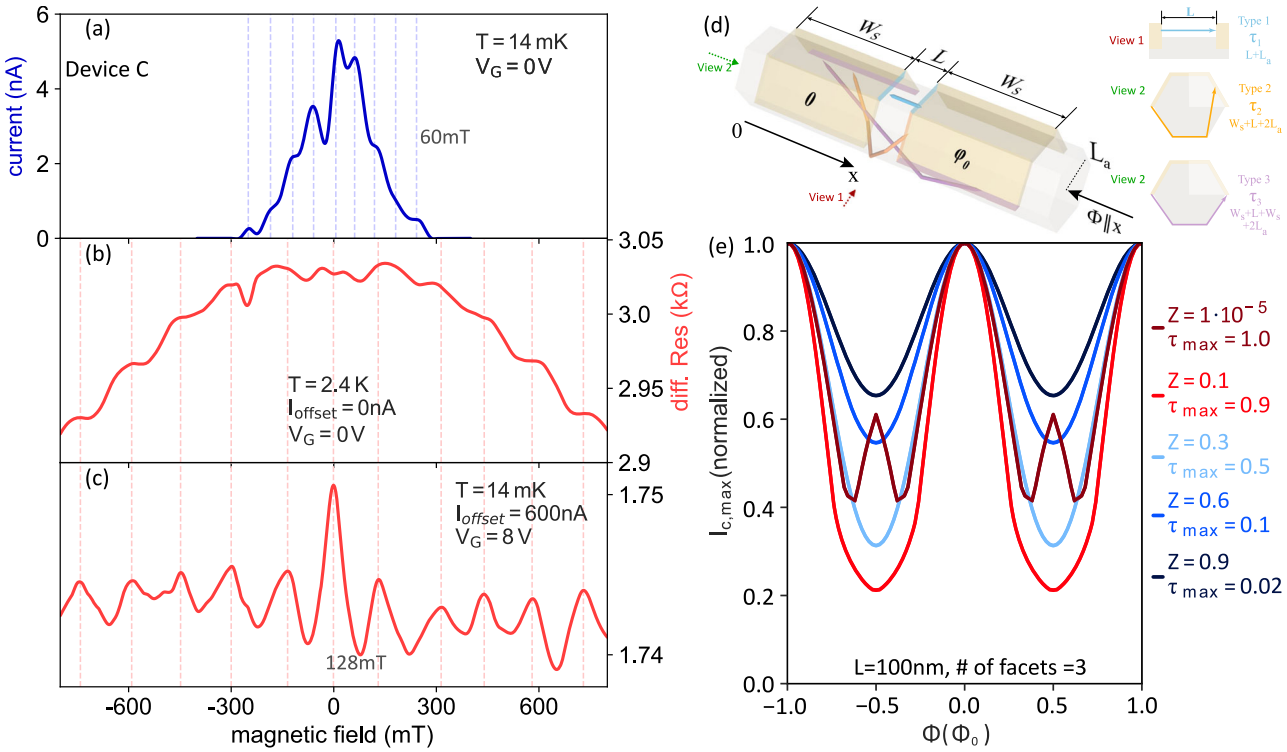

Fig. 5 | Temperature- and bias-dependent evolution of oscillation periodicity and semiclassical interpretation of flux interference. a Switching current of device C measured at $V_g = 0$ V and at $T = 14$ mK. **b** Differential resistance measured at an elevated temperature of 2.4 K and the same gate condition as in (**a**). **c** Differential resistance at $T = 14$ mK and $V_g = 8$ V with a DC current bias of 600 nA, probing transport outside the bias window of the superconducting gap. **d** Schematic depiction of the three possible trajectories on the surface of the hexagonal nanowire. The images at the side show two different perspectives of the system as well as the maximum length scales of the trajectories. The displayed type-2 and type-3 trajectories contribute an AB phase while the type-1 trajectory does not. **e** Example simulation result for a range of dimensionless barrier stengths Z, showing the critical current as a function of magnetic flux, with $\Phi_0 = h/2e$ the magnetic flux quantum. Each trace is also labeled with the maximum value of transparency (τ_{max}) evaluated for all found trajectories.

In a second interpretation, the effect arises from the Josephson junction transport. Here, the oscillations are based on superimposed Andreev reflection trajectories that loop around the perimeter of the InAs shell and enclose magnetic flux. A similar interpretation has recently been employed to explain the magnetic response of topological insulator nanowire Josephson junction devices in which surface states dominate the transport[50]. To illustrate this effect, we utilize a simplified semi-classical model following the work of Himmler et al.[50] in which the different current contributions are integrated over all possible ballistic trajectories[51]. The model used here closely follows the outline by Himmler et al. in ref. 50 and is discussed in detail in the methods section with additional plots in the Supplementary Note 4. Each trajectory represents an electron and hole path, with Andreev reflections occurring at each superconductor interface. Three different types of trajectories can be identified, which differ by the relationship between the angle of incidence (θ_i) at the two relevant superconductor interfaces and the trajectory angle with respect to the wire growth axis (θ_t). Examples of the three trajectory types are shown in Fig. 5c. Type 1 trajectories pass between the two short edges of the superconducting leads at the junction and are therefore equal to the transport situation in a planar system. Type 2 trajectories pass between a short edge of a contact and a long contact edge that is parallel with the nanowire growth direction. Finally, type 3 trajectories pass between two long contact edges. In all cases, it is possible to find trajectories that wind around the nanowire perimeter, enclose a magnetic flux, and induce an AB-type phase shift. We utilize expressions for the Andreev reflection probability taken from the work of Mortensen et al. in ref. 52 to account for the relation between incident angle (θ_i) and the transparency of the channel τ. In Fig. 5e, we use the Blonder and Tinkham model[53] to simulate the device response for different tunnel barrier strength Z. For typical values for nanowire junctions with an epitaxial superconducting shell[35,54], we obtain clear $h/2e$ oscillations that are in accordance with our experimental findings. In the case of very high transparencies, additional $\Phi = \Phi_0/2e$ oscillations can be observed (see Supplementary Note 6), as has been reported in topological insulator nanowires[50]. The most straightforward explanation for the corresponding double peak feature would be the presence of trajectories that make two passes about the circumference of the wire. However, in our simulations, we find that these processes are suppressed due to the angular transparency function and the angular cut-off. Instead, the $\Phi = \Phi_0/2e$ oscillations start to appear due to modifications of the current-phase relation once the system is dominated by type-2 and type-3 trajectories, e.g., if the Z parameter is small and either the length of the channel is increased or the number of facets covered by the superconductor is reduced. Here, the influence of the number of facets covered by superconductor is less intuitive, but stems from a reduction of the angle of incidence, and also a wider range of angle for which highly transmitting trajectories can circle the cylinder before meeting the second lead passing through the gap between the two superconducting leads short edges at least once. However, we would like to stress that we do not see any correlation with phase-winding effects in our simulation and also that we do not detect any experimental signatures of such features in our devices.

Lastly, we investigate the relation between the supercurrent oscillations and the orientation of the magnetic field, i.e., the effect of an off-axis misalignment of the applied magnetic field, on the flux periodicity in device B (see Fig. 6). The oscillation period (ΔB) is extracted from the separation of two peaks close to zero field at $V_g = 4.0$ V and for fields applied in-plane and at an angle θ to the nanowire axis (see Fig. 6a, b) for the experimental data). As shown in Fig. 6c, we observe that an off-axis orientation of the magnetic field leads to an anomalous decrease of the oscillation period. For comparison, the solid red curve in Fig. 6c corresponds to the expected oscillation period assuming that only the axial component of the magnetic field produces the oscillations. This prediction follows a cosine dependence that is

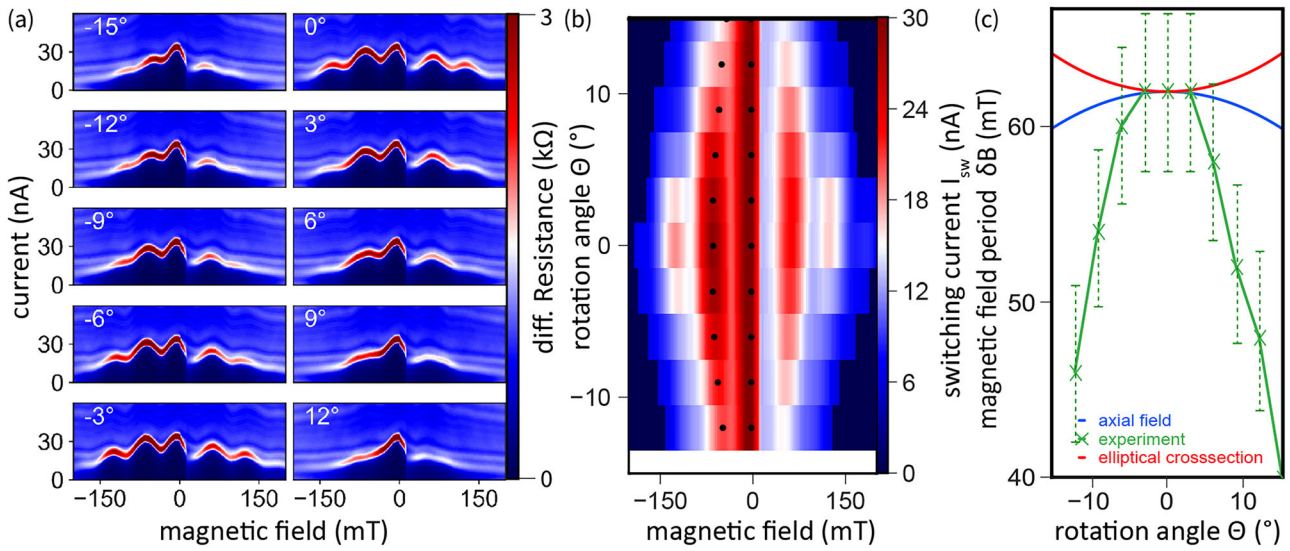

Fig. 6 | Anomalous angular dependence of the oscillation period. Data of field angle dependence for device B at $V_g = 4.0$ V. **a** These plots show the raw data for the plot in (**c**). The color bar is dV/dI with units of kΩ. **b** Switching current I_{sw} as a function of field angle θ from which the magnetic field period ΔB is extracted and plotted in (**c**). **c** The decreasing ΔB is compared with expectations based on flux threading the nanowire axis (red solid line) and threading the elliptical cross section (solid blue line). The error bars correspond to the stepping of the applied magnetic field.

typical for conventional AB-type oscillations, universal conductance fluctuations and weak localization[25,55,56]. We also consider the expected periodicity if the oscillation period was fixed via the flux penetrating the elliptical cross section of the nanowire (shown as a solid blue line in Fig. 6c), which similarly does not reflect the observed dependence. The anomalous angular dependence of the oscillations is a clear indication that the given system can not be described as a simple superconducting AB-type system. However, a similar atypical modification of the oscillation period is observed in the Little-Parks effect in InAs nanowires with full shells of epitaxial aluminum (see Supplementary Note 7) and can most likely be explained by the additional depairing effect of the out-of-plane magnetic field component (see[57] and[58]). Here, the superconducting gap, which acts as the envelope for all Josephson junction-related transport features, is rapidly suppressed. This creates an upper cut-off condition for the supercurrent oscillations and thus an apparent shift of the oscillation maxima towards lower fields.

Conclusions

The study of topological quasiparticles in nanowire-superconductor hybrid structures remains a challenging task due to the strict requirements on the device properties. However, more advanced device layouts such as full-shell nanowire Josephson junctions are a promising approach to loosen the tight margins and make the topological phase space more easily accessible. Here, an essential prerequisite is a fine control of the position of the electron wave function within the conductive area of the nanowire and a strict limitation of the number of radial modes present that are present in the system. This can be achieved by employing GaAs/InAs core/shell nanowires, where the electrons are confined in the narrow InAs quantum well. Indeed, our GaAs/InAs core/shell nanowires equipped with normal contacts revealed pronounced h/e flux-periodic conductance oscillations, which confirm the presence of a tubular channel in the InAs shell. Most importantly, and in contrast to our past work where oscillations were observed either in normal-state conductance[24,34] or finite-voltage Josephson transport[27], we also observe flux-periodic oscillations directly in the Josephson supercurrent, evidencing coherent interference of Andreev bound states in GaAs/InAs core/shell nanowires. By subjecting the system to elevated temperatures and high currents, thereby surpassing the induced proximity gap, we can dynamically switch the oscillation period from $h/2e$ to h/e, transitioning from a two-particle to a single-particle effect. This, paired with the possibility to suppress the oscillatory behavior of the supercurrent by means of an asymmetrically applied gate voltage, as well as the fact that no such oscillations are observed in devices without an etched junction channel, is a clear indication that the effect originates from the superposition and interference of different Andreev reflection processes within the nanowire Josephson junction. We interpret this as clear evidence that the complex, non-trivial geometric topology can indeed be imprinted onto the Andreev transport spectrum in the device and thus be leveraged to adjust and limit the number of radial transport modes. The latter is further confirmed by a semi-classical simulation that investigates the relation between interface transparency, contact geometry, and the resulting oscillations. We also emphasize the absence of signatures associated with the Little-Parks effect, despite the complete proximization of the nanowire channel. This confirms that even a fully proximitized system fundamentally differs from configurations with a fully closed, radially symmetric Al shell, underscoring the significance of partial versus full-shell geometries. We consider the latter an important focus for future research and as a base for devices in which the complex interplay between the number of states, flux quantization, winding of the superconducting order parameter and spin-orbit interaction is precisely tailored, e.g., by further patterning the Al shell, to enhance the topological phase space. This is further supported by compelling evidence for an anomalous relation between magnetic field orientation and oscillation period that can be explained by an enhanced depairing effect and the rapid suppression of the superconducting gap. Our measurements show that GaAs/InAs core/shell nanowires with their non-trivial geometric topology and their ability to limit and adjust the number of radial transport modes are a promising building block for more advanced device concepts, including "hollow nanowire" or "tubular nanowire"/fullshell structures[31–33], and to study topological quasiparticles in nanowire-superconductor hybrid structures. In addition, they provide a template for further investigations regarding the relation between device geometry and the supercurrent oscillations, e.g., the effect of very long junction channels or very short or asymmetric Al contact regions.

Methods

Epitaxial growth

The GaAs/InAs core/shell nanowires are grown by MBE on pre-patterned (111)-Si substrates using the self-catalyzed vapor-liquid-solid method. Prior to the growth, the (111) Si substrates are covered with a 20 nm thick thermally grown SiO_2 layer. This is subsequently patterned via electron beam lithography and reactive ion etching (RIE) to generate a set of hole arrays with different diameters ranging from $d = 40$ to 80 nm and varying hole

pitches of $p = 0.5$, 1, 2 and 4 μm. The preparation procedure can be divided into seven process steps (see ref. 59 for a more detailed description). In step (1), the (111) Si substrates are covered by a 20 nm thick thermally-grown SiO_2 layer as a mask for selective area growth. Subsequently, an ~220 nm thick PMMA-950 K resist layer is spin-coated (2) and afterwards in step (3), the layout is transferred to the PMMA by electron beam lithography. Then, the PMMA layer is developed with AR-600-55 for 70 s and subsequently, the process is stopped by sample immersion in isopropanol for 3 min. The first etching process is conducted by RIE to thin the SiO_2 in the holes down to 1–2 nm thickness using a CHF_3 gas flow of 50 sccm and a RF bias power of 200 W (4). After that, the PMMA layer is removed using acetone, and the patterned substrates are chemically cleaned using Piranha solution and oxygen plasma for 10 min each (5). Directly before loading the sample into the MBE system, it is chemically wet-etched using diluted (1%) HF for another 60 s (6) in order to open the remaining 1–2 nm of SiO_2 in the holes of the pre-patterned substrate. Immediately after the HF dip the samples are loaded in the III/V MBE chamber (7).

The growth procedure of the GaAs/InAs core/shell NWs is initiated by exposure of the pre-patterned substrate to a Ga-flux (about 0.11 μm/h) for 10 min at a growth temperature of 620 °C. During this step, Ga droplets are formed in the holes and act as catalyst particles. Subsequently, the As shutter (BEP(As) = 5×10^{-6} mbar) is opened to start the growth of the GaAs NW core for a duration of about 105 min, which leads to an average NW length of about 4 μm. Since the Ga flux is kept constant all the time, the GaAs core growth is polymorph, i.e., containing segments of wurtzite and cubic crystal stucture along the NW axis. More details on the growth dynamics of such polymorph GaAs NWs on prepatterened substrates are presented in ref. 59. At the end of the GaAs core growth, the sample is exposed for an additional 20 min to the As flux in order to consume the catalyst droplet on top of each nanowire. The GaAs nanowires have a in a typical length of 4 μm and a radius of 100–200 nm. Here, the radius is defined as the distance from the center of the GaAs core to one of the corners of the hexagonal InAs shell.

Subsequently, the InAs shell growth is performed by vapor-solid overgrowth of the GaAs core. Here, an influx of about 0.1 μrmm/h and the same As flux as for the GaAs core growth is applied. The growth temperature is set to 450 °C. In contrast to older studies (see ref. 60), we deposit the InAs using a sequence of four alternating cycles, each composed of 5 min InAs growth (e.g., both shutters, In and As open) and 5 min As-stabilized growth break (e.g., only As open) in order to avoid the formation of a parasitic InAs crystallite on top of the nanowires. The resulting total thickness of the InAs shell is about 20–35 nm.

At the end of the InAs shell growth, the sample is cooled down and in situ transferred to the metal deposition chamber to deposit the Al half shell. No sample rotation is applied for this step and the growth temperature is about −115 °C in order to achieve a smooth Al coverage of the InAs surface. The overall half-shell thickness is about 20–30 nm. Scanning electron micrographs of the grown core/shell nanowires covered with an Al half-shell are shown in Fig. 1a, b. The thickness of InAs shell can be determined directly from these images due to incomplete coverage of the GaAs core at the bottom or top part of the nanowire.

Device fabrication

After the growth, nanowires were transferred from the growth substrate onto a Si(100) substrate. Here, a SEM-based micromanipulator, equipped with a tungsten tip, is used in order to achieve a high level of accuracy. Depending on whether bare core/shell GaAs/InAs or GaAs/InAs/Al half-shell nanowires were characterized, different types of substrates were utilized. In the case of bare core/shell GaAs/InAs nanowire, highly n-doped Si(100) substrates covered with 150 nm of SiO_2 were used. This layer is employed as the gate dielectric, through which the electron density is varied in the nanowire by applying a global back-gate voltage V_g. By means of electron beam lithography and subsequent metalization, Ti/Au contact fingers were defined. Before deposition of the contact fingers, Ar^+ cleaning was applied.

To study the dynamics of Josephson junctions in GaAs/InAs/Al half-shell nanowires, we use the measurement platform introduced in refs. 37,54. The latter is based on highly resistive Si substrates with pre-defined surface gates. The Josephson junction itself is connected through a coplanar-waveguide-type transmission line to an on-chip bias tee, made of an interdigital capacitor and a planar coil. All parts, including the surrounding ground plane, are made of 80 nm thick TiN. To ensure an ohmic connection between NbTi contacts and the Al shell, a fast atom gun (Matsusada Precision FAB-110) was used prior to metal deposition in order to remove the aluminum oxide. The contact separation is chosen to be at least 1.5 μm in order to reduce the impact of the wide-gap superconductor NbTi on the transport through the system.

Transmission electron microscopy

For the side view analysis, the nanowires were transferred from growth arrays to carbon grids by gently rubbing the two surfaces. The cross sections were prepared using focused ion beam (FIB) on nanowires transferred to Si substrates by the very same method. The subsequent TEM analysis was carried out using doubly corrected JEOL ARM 200F and JEOL 2100 microscopes, both operating at 200 kV. The EDX measurements were carried out using an Oxford Instruments 100 mm^2 windowless detector installed within the JEOL ARM 200F.

Electrical measurements

Low-temperature magnetotransport measurements of the core/shell nanowires with normal contacts were carried out in a variable temperature insert cryostat at temperatures between $T = 1.7$ and 20 K, under an axially applied magnetic field up to $B = 4$ T. Biasing with a current $I = 20$ nA between the two outer contacts, measurements were performed in four-terminal configuration by recording the voltage drop with standard lock-in technique between two inner contacts with measurement segment length of 1 μm.

Measurements on Josephson junction devices were performed using a four-terminal setup to the NbTi leads contacting the nanowire. Measurements were performed in a dilution refridgerator with a base temperature of 14 mK, equipped with a two-axis superconducting vector magnet allowing accurate alignment of field parallel to the wire growth axis. Electrical transport measurements were performed using current bias with custom battery-powered electronics (TU Delft QT-IVVI rack) (https://qtwork.tudelft.nl/schouten/ivvi/index-ivvi.htm). Measurements of dV/dI at elevated temperature and higher currents in Fig. 5b, c were performed using standard lock-in techniques with a signal recovery 7270 DSP lock-in amplifier and again the battery-powered IVVI electronics. In contrast to prior results on both normal and superconducting samples[34,42,47], the thin layer of epitaxial Al was rather sensitive to out-of-plane components of the applied field. To address this issue, we performed calibration procedures for both junction devices in which we rotated the magnetic field around the nanowire and thus located the orientation for which the critical field is at its maximum.

Semiclassical model for Josephson junction magnetic response

Here, we employ a semi-classical model adapted from the work of Himmler et al.[50], itself adapting a model from Ostroukh et al.[51]. The model considers classical self-retracing trajectories (Γ) due to pure retro-reflections at interfaces of the superconducting shell in vicinity of the junction. No trajectories arising from normal reflections are considered and as such the model is a significant over-simplification, but nonetheless an useful tool to illustrate the underlying physics of the observed magnetic response. For a full discussion of the model we direct readers to the source in ref. 50, which is only briefly summarized here.

We consider the system pictured in Fig. 5d. Transport is considered to occur on the surface of the hexagonal cross-section nanowire with three of its six facets covered with superconducting aluminum. The hexagonal cross-section of the wire has an apothem of $L_a = 100$ nm. We consider a junction of length $L = 100$ nm and sections of superconducting shell leads of length

$W_S = 1000$ nm. We find all trajectories that pass between the two superconducting regions and assume that each trajectory contributes a current $j(\Gamma)$. The total current is found by integration over all contributions $j(\Gamma)$ for all paths. The junction is assumed to be in the short junction limit, $L \ll \xi = h v_F/\Delta_0$, with v_F the Fermi velocity and Δ_0 the superconducting gap energy. It is useful to define the edge length $L_{edge} = 2L_a/\sqrt{3}$, the perimeter of the nanowire $P = 6L_{edge}$ and the perimeter distance covered by superconductor $C = 3L_{edge}$.

In practice, following Himmler et al.[50], we take a cut through the center of the normal junction region (at $x = W_S + (L/2)$) and characterize all trajectories with a coordinate s along the cut and the axial wave number k_s. The total current is then given by

$$I = \frac{1}{2\pi}\int ds \int dk_s j(s,k_s),$$
$$I = \frac{k_F}{2\pi}\int ds \int d\theta_t \cos(\theta_t) j(s,\theta_t),$$

where θ_t is the angle of the trajectory with respect to the cut line in the z direction around the nanowire cross section perimeter. Each path carries a current given by the expression for the zero-temperature current phase relationship of a short channel junction[61,62],

$$j(\theta_t) = \frac{e\Delta}{4\hbar}\frac{\tau \sin(\varphi_0 - 2\gamma)}{\sqrt{1-\tau\sin^2(\varphi_0/2-\gamma)}},$$

where τ is the transparency for the given trajectory, and $\varphi_0 - 2\gamma$ is the gauge-invariant phase difference[63] which includes the Aharonov–Bohm phase term,

$$\gamma = \frac{e}{\hbar}\int_\Gamma ds \cdot A = n\pi\frac{\Phi}{\Phi_0},$$

with Φ the magnetic flux and $\Phi_0 = h/2e$ the magnetic flux quantum. In practice, the term γ is zero except for trajectories which cross between the source and drain superconductor while traversing the normal region on the underside of the nanowire. Much like Himmler et al.[50], we identify three distinct types of trajectory that differ in details of the angles of incidence at the superconductor interfaces (see examples in Fig. 5d), these are:

- Type 1—Trajectories that begin at $s = W_S$ and end at $s = W_S + L$. These trajectories have the same angle of incidence θ_i on both superconducting leads.
- Type 2—Trajectories with one end at the short edge of the superconducting leads (at $s = W_S$ or $s = W_S + L$) and one end along the long edge of the superconducting lead ($z = 0$ or $z = C$).
- Type 3 - Trajectories that both begin and end at the long edge of the superconducting leads ($z = 0$ or $z = C$).

These three types differ in terms of the angle of incidence θ_i of the trajectory with the superconductor interface and its relationship with the trajectory angle θ_t. In contrast to the work of Himmler et al.[50], we use expressions for the angular dependence of Andreev reflection probabilities at semiconductor-superconductor interfaces taken from Mortensen et al.[52] in order to evaluate the transparencies (τ) of each trajectory. From ref. 52, we describe the transparency as $|A(\theta_{i,source})A(\theta_{i,drain})|$ where $A(\theta_{i,m})$ is the Andreev reflection probability at the start or end interface of the trajectory given as

$$A(\theta_{i,m}) = \frac{1}{\tilde{E}^2 + (1-\tilde{E}^2)(1+2Z_{eff}^2(\theta_{i,m}))^2} \text{ for } \theta_{i,m} < \theta_c,$$
$$A(\theta_{i,m}) = 0 \text{ for } \theta_{i,m} \geq \theta_c,$$

where $\tilde{E} = E/\Delta_0$ is the normalized energy and Z_{eff} is an effective tunnel barrier strength given as

$$Z_{eff}(\theta_{i,m}) = \sqrt{\kappa(\theta_{i,m})\left(\frac{Z}{\cos\theta_{i,m}}\right)^2 + \frac{(\kappa(\theta_{i,m})r_v - 1)^2}{4\kappa(\theta_{i,m})r_v}},$$

where $Z = U_0/\hbar\sqrt{v_F^N v_F^S}$ is the dimensionless barrier strength introduced by Blonder and Tinkham[53], with U_0 the barrier height, and $r_v = v_F^N/v_F^S$ is the ratio of Fermi velocities in the normal conductor and in the superconductor. The term $\kappa(\theta_{i,m})$ is given as

$$\kappa(\theta_{i,m}) = \cos/\sqrt{1 - r_k^2\sin^2(\theta_{i,m})},$$

where $r_k = k_F^N/k_F^S$ the ratio of wave numbers in the normal conductor and superconductor. The critical incident angle $\theta_c = \arcsin(1/r_k)$ has the effect of cutting off contributions of many trajectories. The critical angle accounts for the suppression of the Andreev reflection probability when momentum cannot be conserved due to the parallel momentum in the normal region exceeding the Fermi momentum of the superconductor. For additional discussion of the modeling and simulation results under different conditions see the Supplementary Notes 6 and 7. In all simulations we have assumed that $r_v = r_k = 1$.

Data availability

All the data that support the plots and the other findings of this study are available from the corresponding author upon reasonable request.

Received: 15 April 2024; Accepted: 27 July 2025;
Published online: 01 September 2025

References

1. Tosi, L. et al. Spin-orbit splitting of Andreev states revealed by microwave spectroscopy. *Phys. Rev. X* **9**, 011010 (2019).
2. Metzger, C. et al. Circuit-QED with phase-biased Josephson weak links. *Phys. Rev. Res.* **3**, 013036 (2021).
3. Zellekens, P. et al. Microwave spectroscopy of Andreev states in InAs nanowire-based hybrid junctions using a flip-chip layout. *Commun. Phys.* **5**, 267 (2022).
4. Zazunov, A. et al. Andreev level qubit. *Phys. Rev. Lett.* **90**, 087003 (2003).
5. Zazunov, A., Shumeiko, V. S., Wendin, G. & Bratus', E. N. Dynamics and phonon-induced decoherence of Andreev level qubit. *Phys. Rev. B* **71**, 214505 (2005).
6. van Woerkom, D. J. et al. Microwave spectroscopy of spinful Andreev bound states in ballistic semiconductor Josephson junctions. *Nat. Phys.* **13**, 876 (2017).
7. Hays, M. et al. Coherent manipulation of an Andreev spin qubit. *Science* **373**, 430 (2021).
8. Cerrillo, J., Hays, M., Fatemi, V. & Yeyati, A. L. Spin coherent manipulation in Josephson weak links. *Phys. Rev. Res.* **3**, L022012 (2021).
9. Sarma, S. D., Freedman, M. & Nayak, C. Majorana zero modes and topological quantum computation. *npj Quantum Inf.* **1**, 1 (2015).
10. Oreg, Y., Refael, G. & von Oppen, F. Helical liquids and Majorana bound states in quantum wires. *Phys. Rev. Lett.* **105**, 177002 (2010).
11. Lutchyn, R. M., Sau, J. D. & Das Sarma, S. Majorana fermions and a topological phase transition in semiconductor-superconductor heterostructures. *Phys. Rev. Lett.* **105**, 077001 (2010).
12. Kitaev, A. Fault-tolerant quantum computation by anyons. *Ann. Phys.* **303**, 2 (2003).
13. Vaitiekėnas, S. et al. Topological superconductivity in full shell proximitized nanowires. *Science* **367**, eaav3392 (2020)

14. Stanescu, T. D., Sitek, A. & Manolescu, A. Robust topological phase in proximitized core-shell nanowires coupled to multiple superconductors. *Beilstein J. Nanotechnol.* **9**, 1512 (2018).
15. Vaitiekėnas, S., Krogstrup, P. & Marcus, C. M. Anomalous metallic phase in tunable destructive superconductors. *Phys. Rev. B* **101**, 060507 (2020).
16. Lesser, O. & Oreg, Y. Majorana zero modes induced by superconducting phase bias. *J. Phys. D Appl. Phys.* **55**, 164001 (2022).
17. Little, W. A. & Parks, R. D. Observation of quantum periodicity in the transition temperature of a superconducting cylinder. *Phys. Rev. Lett.* **9**, 9 (1962).
18. San-Jose, P., Payá, C., Marcus, C. M., Vaitiekėnas, S. & Prada, E. Theory of caroli–de Gennes–Matricon analogs in full-shell hybrid nanowires. *Phys. Rev. B* **107**, 155423 (2023).
19. Svetogorov, A. E., Loss, D. & Klinovaja, J. Enhancement of the Kondo effect in a quantum dot formed in a full-shell nanowire. *Phys. Rev. B* **107**, 134505 (2023).
20. Peñaranda, F., Aguado, R., San-Jose, P. & Prada, E. Even-odd effect and Majorana states in full-shell nanowires. *Phys. Rev. Res.* **2**, 023171 (2020).
21. Valentini, M. et al. Nontopological zero-bias peaks in full-shell nanowires induced by flux-tunable Andreev states. *Science* **373**, 82 (2021).
22. Kringhøj, A. et al. Andreev modes from phase winding in a full-shell nanowire-based transmon. *Phys. Rev. Lett.* **126**, 047701 (2021).
23. Woods, B. D., Das Sarma, S. & Stanescu, T. D. Electronic structure of full-shell InAs/Al hybrid semiconductor-superconductor nanowires: Spin-orbit coupling and topological phase space. *Phys. Rev. B* **99**, 161118 (2019).
24. Gül, O. et al. Flux periodic magnetoconductance oscillations in GaAs/InAs core/shell nanowires. *Phys. Rev. B* **89**, 045417 (2014).
25. Haas, F. et al. Angle-dependent magnetotransport in GaAs/InAs core/shell nanowires. *Sci. Rep.* **6**, 24573 (2016).
26. Haas, F. et al. Electron interference in Hall effect measurements on GaAs/InAs core/shell nanowires. *Nano Lett.* **17**, 128 (2017).
27. Haas, F. et al. Anisotropic phase coherence in GaAs/InAs core/shell nanowires. *Nanotechnology* **28**, 445202 (2017).
28. Kloeffel, C., Rančić, M. J. & Loss, D. Direct Rashba spin-orbit interaction in Si and Ge nanowires with different growth directions. *Phys. Rev. B* **97**, 235422 (2018).
29. Wójcik, P., Bertoni, A. & Goldoni, G. Enhanced Rashba spin-orbit coupling in core-shell nanowires by the interfacial effect. *Appl. Phys. Lett.* **14**, 073102 (2019).
30. Furthmeier, S. et al. Enhanced spin-orbit coupling in core/shell nanowires. *Nat. Commun.* **7**, 12413 (2016).
31. Giavaras, G. & Aguado, R. Flux-tunable supercurrent in full-shell nanowire Josephson junctions. *Phys. Rev. B* **109**, 024509 (2024).
32. Payá, C. et al. Phenomenology of Majorana zero modes in full-shell hybrid nanowires. *Phys. Rev. B* **109**, 115428 (2024).
33. Payá, C., Aguado, R., San-Jose, P. & Prada, E. Josephson effect and critical currents in trivial and topological full-shell hybrid nanowires, *Phys. Rev. B.* **111**, 235420 (2025).
34. Haas, F. et al. Quantum interferometer based on GaAs/InAs core/shell nanowires connected to superconducting contacts. *Semicond. Sci. Technol.* **33**, 064001 (2018).
35. Krogstrup, P. et al. Epitaxy of semiconductor–superconductor nanowires. *Nat. Mater.* **14**, 400 (2015).
36. Güsken, N. A. et al. Mbe growth of Al/InAs and Nb/InAs superconducting hybrid nanowire structures. *Nanoscale* **9**, 16735 (2017).
37. Perla, P. et al. Fully in situ NB/InAs-nanowire Josephson junctions by selective-area growth and shadow evaporation. *Nanoscale Adv.* **3**, 1413 (2021).
38. van der Wiel, W. G. et al. Electromagnetic Aharonov-Bohm effect in a two-dimensional electron gas ring. *Phys. Rev. B* **67**, 033307 (2003).
39. Octavio, M., Tinkham, M., Blonder, G. E. & Klapwijk, T. M. Subharmonic energy-gap structure in superconducting constrictions. *Phys. Rev. B* **27**, 6739 (1983).
40. Flensberg, K., Hansen, J. B. & Octavio, M. Subharmonic energy-gap structure in superconducting weak links. *Phys. Rev. B* **38**, 8707 (1988).
41. Zellekens, P. et al. Phase coherent transport and spin-orbit interaction in GaAs/InSb core/shell nanowires. *Semicond. Sci. Technol.* **35**, 085003 (2020).
42. Gül, O. et al. Giant magnetoconductance oscillations in hybrid superconductor-semiconductor core/shell nanowire devices. *Nano Lett.* **14**, 6269–6274 (2014).
43. Ibabe, A. et al. Joule spectroscopy of hybrid superconductor–semiconductor nanodevices. *Nat. Commun.* **14**, 2873 (2023).
44. Stampfer, L. et al. Andreev interference in the surface accumulation layer of half-shell InAsSb/Al hybrid nanowires. *Adv. Mater.* **34**, 2108878 (2022).
45. Sato, Y. et al. Quasiparticle trapping at vortices producing Josephson supercurrent enhancement. *Phys. Rev. Lett.* **128**, 207001 (2022).
46. Al'tshuler, B. L., Aronov, A. G. & Spivak, B. Z. Aharonov-Bohm effect in disordered conductors. *JETP Lett.* **33**, 101 (1981).
47. Günel, H. Y. et al. Supercurrent in Nb/InAs-nanowire/Nb Josephson junctions. *J. Appl. Phys.* **112**, 034316 (2012).
48. Nikulov, A. V. & Zhilyaev, I. N. The little-parks effect in an inhomogeneous superconducting ring. *J. Low. Temp. Phys.* **112**, 227 (1998).
49. Sharon, O. J., Shaulov, A., Berger, J., Sharoni, A. & Yeshurun, Y. Current-induced squid behavior of superconducting Nb nano-rings. *Sci. Rep.* **6**, 28320 (2016).
50. Himmler, W. et al. Supercurrent interference in hgte-wire Josephson junctions. *Phys. Rev. Res.* **5**, 043021 (2023).
51. Ostroukh, V. P., Baxevanis, B., Akhmerov, A. R. & Beenakker, C. W. J. Two-dimensional Josephson vortex lattice and anomalously slow decay of the Fraunhofer oscillations in a ballistic SNS junction with a warped Fermi surface. *Phys. Rev. B* **94**, 094514 (2016).
52. Mortensen, N. A., Flensberg, K. & Jauho, A.-P. Angle dependence of Andreev scattering at semiconductor–superconductor interfaces. *Phys. Rev. B* **59**, 10176 (1999).
53. Blonder, G. E. & Tinkham, M. Metallic to tunneling transition in Cu-Nb point contacts. *Phys. Rev. B* **27**, 112 (1983).
54. Zellekens, P. et al. Hard-gap spectroscopy in a self-defined mesoscopic InAs/Al nanowire Josephson junction. *Phys. Rev. Appl.* **14**, 054019 (2020).
55. Jespersen, T. S., Hauptmann, J. R., Sørensen, C. B. & Nygård, J. Probing the spatial electron distribution in InAs nanowires by anisotropic magnetoconductance fluctuations. *Phys. Rev. B* **91**, 041302 (2015).
56. Liang, D., Du, J. & Gao, X. P. A. Anisotropic magnetoconductance of a inas nanowire: angle-dependent suppression of one-dimensional weak localization. *Phys. Rev. B* **81**, 153304 (2010).
57. Vekris, A. et al. Asymmetric little-parks oscillations in full shell double nanowires. *Sci. Rep.* **11**, 19034 (2021).
58. Rogachev, A., Bollinger, A. T. & Bezryadin, A. Influence of high magnetic fields on the superconducting transition of one-dimensional nb and moge nanowires. *Phys. Rev. Lett.* **94**, 017004 (2005).
59. Jansen, M. M. et al. Phase-pure wurtzite GaAs nanowires grown by self-catalyzed selective area molecular beam epitaxy for advanced laser devices and quantum disks. *ACS Appl. Nano Mater.* **3**, 11037 (2020).
60. Rieger, T., Luysberg, M., Schäpers, T., Grützmacher, D. & Lepsa, M. I. Molecular beam epitaxy growth of GaAs/InAs core-shell nanowires and fabrication of InAs nanotubes. *Nano Lett.* **12**, 5559 (2012).
61. Beenakker, C. W. J. Universal limit of critical-current fluctuations in mesoscopic Josephson junctions. *Phys. Rev. Lett.* **67**, 3836 (1991).
62. Klapwijk, T. Proximity effect from an Andreev perspective. *J. Supercond.* **17**, 593 (2004).

63. Tinkham, M. *Introduction to Superconductivity* (Dover Publications, 2004)
64. Albrecht, W., Moers, J. & Hermanns, B. HNF-Helmholtz Nano Facility. *J. Large Scale Res. Facil.* **3**, 112 (2017).

Acknowledgements

We thank Herbert Kertz for technical assistance and Vladan Brajovic for help with sample characterization. Dr. Florian Lentz, Dr. Stefan Trellenkamp, and Rainer Benczek are gratefully acknowledged for their help with the required e-beam lithography and deposition of the superconducting material. We thank Andrei Manolescu, Mikio Eto, and Rui Sakano for fruitful discussions. Most of the fabrication has been performed in the Helmholtz Nano Facility at Forschungszentrum Jülich[64]. This work was partly funded by Deutsche Forschungsgemeinschaft (DFG, German Research Foundation) under Germany's Excellence Strategy-Cluster of Excellence Matter and Light for Quantum Computing (ML4Q) EXC 2004/1-390534769. This work was supported by JSPS Grants-in-Aid for Scientific Research (S) (No. 19H05610), JSPS Kakenhi (No. 19H00867) and a SPDR Fellowship provided by the "Young Scientist Program". The work in RIKEN and Julich was supported by Japan Science and Technology Agency (JST) ASPIRE program (Grant number: JPMJAP2338).

Author contributions

B.B., C.K., and A.P. performed the nanowire growth by MBE and the deposition of the superconducting shell. F.B. and E.Z. prepared the substrates for the nanowire growth, fabricated the samples without a superconducting shell and carried out the normal transport measurements. R.S.D., P.Z., and M.D.R. prepared the device chips for the DC and AC junction measurements and fabricated the Josephson junctions. R.S.D. and P.Z. carried out the low-temperature experiments on Josephson junctions and the subsequent data analysis. R.J. and A.M.S. carried out the TEM and EDX studies. P.Z., F.B., A.P., R.S.D., D.G., K.I., and T.S. wrote the manuscript. All authors contributed to the discussions.

Competing interests

The authors declare no competing interests.

Additional information

Supplementary information The online version contains supplementary material available at https://doi.org/10.1038/s42005-025-02242-7.

Correspondence and requests for materials should be addressed to Patrick Zellekens.

Peer review information *Communications Physics* thanks the anonymous reviewers for their contribution to the peer review of this work.